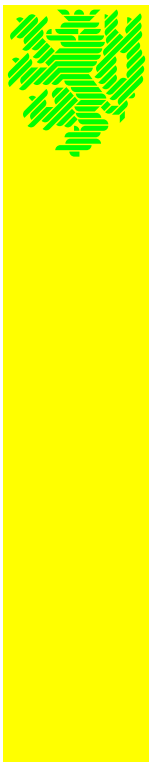

Bergische Universität Wuppertal
Fakultät für
Mathematik und Naturwissenschaften
Fachgruppe Physik

Master Praktikum

FP1

Stern-Gerlach Experiment

Alexander Adam 1946255
Felix Orda 1948680
Philip Rouenhoff 1620118

Abstract

The famous Stern-Gerlach experiment is conducted using potassium atoms. Due to the electron configuration of potassium the quantization of the electron spin can be demonstrated. In addition the Landé factor, the gyromagnetic factor of the electron, is measured to be

$$g_e^{\text{total}} = 1.16 \pm 0.16.$$

which poses a deviation to the literature value of 72 %, resp. 5.26σ. Lastly the enthalpy of vaporization of potassium is determined as (0.43 ± 0.03) eV, which significantly deviates from the literature.

Betreuer: Sukyung Kim, M. Sc.

Durchgeführt am: 15. Jan. 2024
Vorgesehene Protokollabgabe: 29. Jan. 2024
Abgabedatum: 29. Jan. 2024

Bewertung Protokoll	max. %	+/0/-	erreicht %
Formales	6		
Einleitung & Theorie	6		
Durchführung Auswertung phys. Diskussion Zusammenfassung	33		
Qualität der Messung	15		

Contents

1 Introduction **3**

2 Theoretical Foundations **4**
2.1 Spin of Elementary Particles 4
2.2 Deflection of a Potassium Ray in a Stern-Gerlach Apparatus 5

3 Experimental Setup **6**

4 Measurements and Analysis **10**
4.1 The Atomic Ray 10
4.2 Configuration of the Langmuir-Taylor Detector 11
4.3 Measurement of the Ray Profile and Splitting 12
4.4 Measurement of the Vapor Pressure of Potassium 17

5 Summary **19**

A Further Data **20**

B Full Measurements **23**

C Gaussian Error Propagation **26**

List of Figures

1 Most probable trajectory of potassium in SG apparatus 7
2 Sketch of Ealing-Daybell SG experiment 7
3 Sketch of magnetic field in SG apparatus 8
4 Sketch of Langmuir-Taylor detector 8
5 Magnetization curve of a magnet which is subject to the process of pulse degaussing 9
6 Logarithmic plot of the raw measurements of signal intensity with and without the beam activated 11
7 Linear plot of the signal to noise ratio 12
8 Fit of the resolution function 13
9 Plot to determine the relativ and abolut erros 14
10 Beam intensity measurement at $(0.329 \pm 0.021)\,\mathrm{T}$ 15
11 Repeated beam intensity measurement at $(0.329 \pm 0.021)\,\mathrm{T}$ 15
12 Beam intensity measurement at $(0.501 \pm 0.038)\,\mathrm{T}$ 16
13 Fit of the measured data with the Clausius-Clayperon equation 18
A.1 Fitting of the temperature resistance curve 20
A.2 Fitting of the magnetic field and current curve 20
A.3 Linear plot of the signal to noise ratio 21
A.4 Linear plot of the raw measurements of signal intensity with and without the beam activated 21
A.5 Raw data recorded while the heating current was set to 950 mA 22
A.6 Measurement taken directly taken after a long burn 22

List of Tables

1 Measured values of g_e^{naive} 16
2 Measured values of g_e 17
B.1 Measurement series for the signal to noise ratio 23
B.2 Data form the measurement of the ray profile and splitting 24
B.3 Measurement series of the cooling down of the oven 25

1 Introduction

During this laboratory course experiment the Stern-Gerlach experiment will be conducted. This famous and often quoted experiment that lead to the original publications [1, 2] by Stern and Gerlach showed the quantization of the spin of the electron and allows to measure electron's gyromagnetic factor g_e. While the original experiment used a ray of silver atoms, the modified Ealing-Daybell Stern-Gerlach apparatus used throughout this lab course is operated with potassium. This allows in addition to measure the vapor pressure of potassium.

In the night from 7 to 8 February 1922 [3], the physicists Otto Stern and Walter Gerlach demonstrated that unpolarized silver atoms in the ground state with a finite momentum inside an inhomogeneous magnetic field experience a force. This force accelerates the atoms along a direction perpendicular to their momentum *and* in the very opposite direction with equal probability. This force had to be the result of a magnetic dipole moment of the silver atom. However, since the electron configuration of silver is such that the net orbital angular momentum of the electrons amounts to zero, the source of the observed magnetic moment was still missing. It was Goudsmit and Uhlenbeck who later, in 1925, conjectured that the electron has an intrinsic angular momentum, the so-called spin. With this theory it was possible in hindsight to interpret the outcome of the Stern-Gerlach experiment as stated above: the electron has an intrinsic angular momentum, and it is quantized. [4]

The gyromagnetic factor of the electron g_e, also known as the Landé factor, describes the ratio between the classically expected magnetic moment caused by its spin and that which is actually observed. The measurement of the gyromagnetic factor of elementary particles is still an interesting endeavor up to this day. Most prominently, in recent years the anomalous magnetic moment of the muon, defined as $\frac{g_\mu - 2}{2}$, has been in the center of attention in the community of particle physics, with g_μ being the gyromagnetic factor of the muon (an elementary particle which, apart from its mass and other minor details, shares a lot of the properties of the electron to say the least, especially regarding the spin [5]). Considerable investigative efforts have been made both experimentally as well as theoretically in order to precisely determine this quantity. The reason behind this were slight deviations of the measured anomalous magnetic moment, measured by Fermilab [6, 7, 8], to the hitherto known theoretical predictions, hinting at new physics. However, by means of lattice gauge theory, the BMW-collaboration (Budapest, Marseilles, Wuppertal, [9]) produced a theoretical prediction which significantly alleviated the alleged tension between experiment and theory. In summary: the topic treated within the scope of this lab course experiment has prominent relevance historically as well as today.

This protocol is organized as follows: in Section 2 the theoretical basics needed for this experiment are discussed. In Section 3 the setup of the experiment is described and the strategy of measurement is explained. Section 4 describes the execution of the experiment and analysis of the data. Finally, a brief summary is given in Section 5.

2 Theoretical Foundations

In this section the theoretical background necessary for the conduction of the experiment is elucidated. If not stated otherwise, the sources used for the information provided are either the textbook [4] or the exemplary protocol [10] provided as part of the lab course.

In Section 2.1 the fundamentals regarding quantum mechanical spin are explained, and in Section 2.2 the deflection of particles with a quantum mechanical magnetic moment in an inhomogeneous magnetic field is portrayed.

2.1 Spin of Elementary Particles

Spin is an intrinsic property of elementary particles that cannot be understood from a classical perspective. It causes the elementary particle to behave as though it had an *intrinsic* angular momentum (as opposed to an *orbital* angular momentum) in the sense that a charged particle with spin has an intrinsic magnetic moment $\vec{\mu}$, similar to that of a closed conductor loop through which an electric current runs. This magnetic moment can be measured during an experiment and is calculated via

$$\vec{\mu} = g\frac{q}{2m}\vec{s}, \tag{1}$$

where $\vec{s}$ is the spin vector of the elementary particle, q its charge, m its mass and g its gyromagnetic factor, or Landé factor (more on that below). Specifically for the electron we know that it has a spin of $\pm\frac{\hbar}{2}$, which means that if one component of either s_x, s_y or s_z of the spin is measured, it can take the values of $\pm\frac{\hbar}{2}$ with equal probability. [1] One thus says that the electron is a spin-$\frac{1}{2}$ particle and introduces the spin quantum number s as well as a magnetization quantum number $m_s \in \{-s, -s+1, ..., s-1, s\}$. In the case of the electron it is $s = \frac{1}{2}$ and $m_s = \pm\frac{1}{2}$.

In other words, spin is quantized, a prominent feature of some observables in quantum mechanics. [2] Using furthermore that $q = e$, the elementary charge, and plugging in the mass of the electron m_e and its gyromagnetic factor g_e, we can write for any spin component s_i, $i \in \{x, y, z\}$:

$$\mu_i = g_e\frac{e}{2m_e}s_i = g_e\frac{e\hbar}{2m_e}m_s = g_e\mu_B m_s = \pm\frac{1}{2}g_e\mu_B, \tag{2}$$

where we introduced the Bohr magneton $\mu_B = \frac{e\hbar}{2m_e} = 9.274\,015(3) \times 10^{-24}\,\mathrm{J/T}$ [4].

The gyromagnetic factor g_e is a dimensionless constant. While the Dirac-Pauli equation predicts $g_e = 2$ (after some approximations) [11], the experimentally measured value is $g_e = 2.002\,319\,304\,362\,2(15)$ [4].

[1] Of course, the experiment that supports this claim is famously the Stern-Gerlach experiment to be recreated in this lab course.

[2] Another such feature is the so called non-commutativity of some observables, such as that of two different spin components. This phenomenon manifests when measuring e.g. first s_x, then s_y and then s_x again. It need not be that the second measurement of s_x gives the same result as the first! This could, in theory, be examined using two Stern-Gerlach apparatuses, which, unfortunately, is not possible with the given equipment.

2.2 Deflection of a Potassium Ray in a Stern-Gerlach Apparatus

Now consider an external magnetic field $\vec{B}$. From electrodynamics we know that a magnetic moment in such an external field has the potential energy of

$$V(\vec{x}) = -\vec{\mu}\vec{B}(\vec{x}), \tag{3}$$

yielding a force of

$$\vec{F}(\vec{x}) = -\vec{\nabla}V = \mu_z \, \partial_z B_z \vec{e}_z, \tag{4}$$

where we approximated that $\vec{B} = (0, 0, B_z)^{\mathrm{T}}$ (which is a good approximation for our experiment, for more on that see Section 3). Hence an electron that enters an inhomogeneous magnetic field experiences an acceleration. Now the electron configuration of potassium is such that all orbitals are filled up except for the $4s^1$ orbital, in which one electron resides. As a consequence the total angular momentum of all electrons of potassium is that of the one electron from the $4s^1$ orbital, which is its spin (because all s-electrons have an orbital angular momentum quantum number of $l = 0$). As we can see from Equation (1), due to its significantly larger mass the nucleus does not contribute much to the overall magnetic moment compared to the contribution of the electron. This means that the overall magnetic moment of the potassium atom is in good approximation the spin of the electron.

Now consider a potassium beam that travels through an inhomogeneous magnetic field whose gradient only has net contributions from the z-component (at least in the place which the beam travels through). The situation is depicted in Figure 1, and again the reason for these assumptions is given in Section 3. If the beam travels with velocity v in a direction orthogonal to z along a distance of d_1 inside the magnetic field and after that for a distance of d_2 outside the field, the distance traveled in z-direction will accumulate to

$$z(v) = \frac{1}{v^2}\left(\mu_z[\partial_z B_z]\frac{d_1}{M}\left[\frac{d_1}{2} + d_2\right]\right), \tag{5}$$

where M is the mass of a potassium atom. The potassium beam is produced by means of an oven, inside of which the velocity of the atoms is distributed according to the Maxwell-Boltzmann distribution

$$f(v) = \sqrt{\frac{2}{\pi}}\left(\frac{M}{k_B T}\right)^{\frac{3}{2}} v^2 \, e^{\frac{-Mv^2}{2k_B T}} \tag{6}$$

with the Boltzmann constant k_B and the oven temperature T, from which the most probable velocity v_0 can be computed to be

$$v_0 = \sqrt{\frac{2k_B T}{M}}. \tag{7}$$

One can now define a deflection $z_0 = z(v_0)$, and using Equations (2), (5) and (7) we can compute it as

$$z_0 = \pm\frac{1}{2} g_e \mu_B [\partial_z B_z] d_1 \, \frac{d_1 + 2d_2}{4k_B T}. \tag{8}$$

The overall intensity distribution is expected to be [10]

$$h\left(\frac{z}{z_0}\right) = \left(\frac{z_0}{z}\right)^3 e^{\frac{-z_0}{z}}, \tag{9}$$

which has a maximum at $\frac{z_{\max}}{z_0} = \frac{1}{3}$. Note that $z_{\max} \neq z_0$ because the probability $g(v)$ for an atom to exit the oven is also proportional to v, i.e.

$$g(v) \propto v \cdot f(v). \tag{10}$$

Using the above information one can determine the Landé factor by plugging in for z_0:

$$\begin{aligned} & z_0 = 3z_{\max} \\ \iff \quad & 3z_{\max} = \pm\frac{1}{2} g_e \mu_B [\partial_z B_z] d_1 \, \frac{d_1 + 2d_2}{4k_B T} \\ \iff \quad & g_e = \left| \frac{24 z_{\max} k_B T}{\mu_B [\partial_z B_z] d_1 (d_1 + 2d_2)} \right| \end{aligned} \tag{11}$$

At this point it is worth mentioning that, due to the resolution $R(z)$ of the detector, the data obtained will be compared to the convolution of the resolution and the intensity distribution

$$h_{\text{meas}}(z) = (h * R)(z) = \int_{-\infty}^{\infty} h(\tilde{z}) R(z - \tilde{z}) \, \mathrm{d}\tilde{z}, \tag{12}$$

compare e.g. [12, 13]. The specific formula of the Voigt resolution function is given below at the end of Section 3 as Equation (16). Here we want to motivate the necessity for the convolution as shown above: if a particle is registered at the detector, it will appear at location z with probability $h(z)$. However, due to the finite resolution R of the detector it may be detected elsewhere in the vicinity of $h(z)$. During the experiment the situation is somewhat reversed; here a particle is detected at some location, i.e. it is $h_{\text{meas}}(z)$ that is measured, and it could have actually hit the detector at some place in the vicinity of $h_{\text{meas}}(z)$. To account for this effect in a continuous manner, the convolution in Equation (12) is needed. A helpful visual explanation is given in the corresponding Wikipedia article.[3]

3 Experimental Setup

In this section the experimental setup will be elaborated upon. The main sources for this section are [10, 14].

The apparatus used throughout this experiment is a modified Ealing-Daybell Stern-Gerlach apparatus, a detailed description of which can be found in [14]. A sketch of this setup can be found in Figure 2. The inside of the apparatus is evacuated using a turbopump. The potassium ray is generated using an oven that is heated by means of electrical resistors. Inside the oven metallic potassium gets vaporized and exits the oven through an aperture. It can be opened and closed by holding a rod magnet next to it and is linked to a cold trap, which has to be refilled with liquid nitrogen throughout the experiment and further helps in keeping a clean vacuum. After that the ray goes through another aperture, further narrowing the ray's profile. It then proceeds to travel through the pole pieces of an electromagnet, the geometry of which can be seen in Figure 3 and will be further elaborated upon below, for it is this part of

[3] The link referenced is https://en.wikipedia.org/wiki/Convolution#Visual_explanation (visited on Jan. 27, 2024).

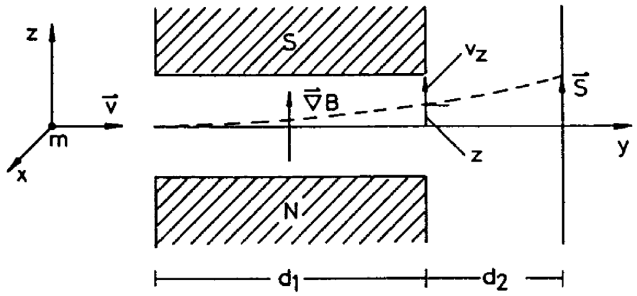

Figure 1: *An example of the most probable trajectory of potassium atoms inside the Stern-Gerlach apparatus. It is* $d_1 = 10.16\,\mathrm{cm}$ *and* $d_2 = 40.00\,\mathrm{cm}$*. Both distances and the sketch are from [15], where the distances are given without uncertainty.*

the apparatus in which the deflection of the ray takes place. Finally, after covering the distance d_2 outside of the magnetic field, the ray hits a Langmuir-Taylor (LT)-detector, a sketch of which can be found in Figure 4. The operating principle of the LT-detector will also be further explained below.

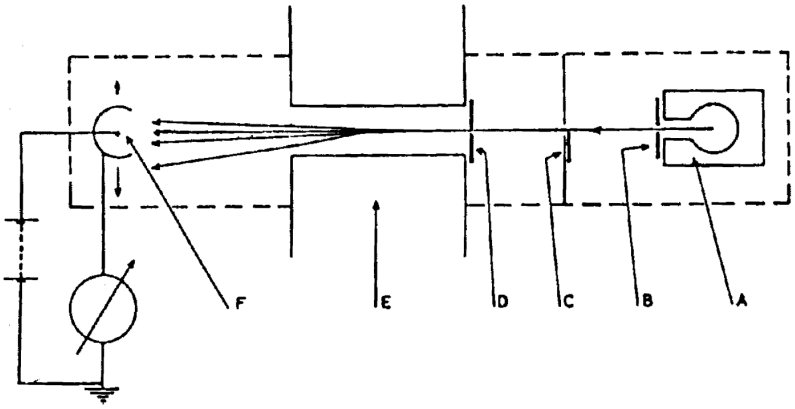

Figure 2: *Sketch of the Ealing-Daybell Stern-Gerlach experiment. [14]*
A: oven
B: aperture for the oven
C: aperture with cold trap
D: ray aperture
E: pole pieces (length: $d_1 = 10.16\,\mathrm{cm}$*, cf. Figure 1)*
F: Langmuir-Taylor detector
D →F: $d_1 + d_2 = 50.16\,\mathrm{cm}$

Regarding the pole pieces, in Figure 3 one can see their geometry and a sketch of the magnetic field generated by them. As described in Section 2.2, in the place the ray travels through the gradient of the field only has a non-vanishing contribution from the z-component. It is approximately given via

$$\partial_z B_z = C B_z \quad \text{where} \quad C \approx 174.42\,\mathrm{m}^{-1}, \tag{13}$$

but due to a decline of the divergence with growing $|y|$ (the direction orthogonal to both the beam direction and the direction of displacement, cf. Figure 3) a correction

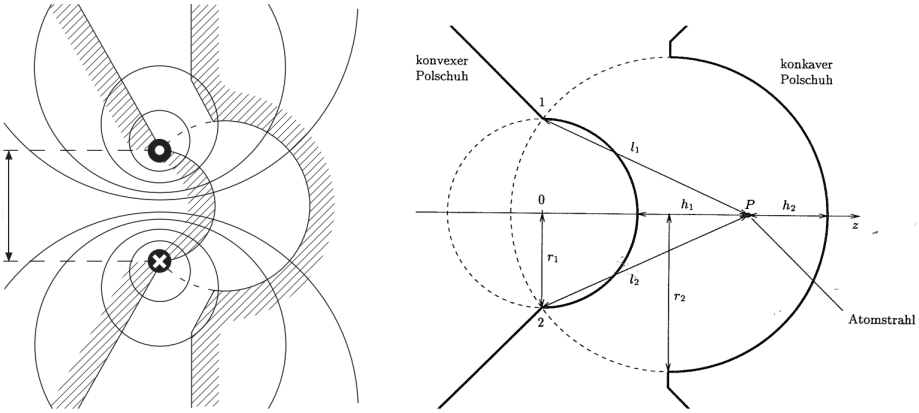

Figure 3: ***Left:*** *sketch of magnetic field lines of the pole shoes (the wires whose cross sections are shown are not part of the setup; they are drawn because they produce a magnetic field equivalent to that of the pole shoes).*
Right: *profile of the pole pieces for the magnets.*
The German words translate as follows: „konvexer / konkaver Polschuh“*: "convex / concave pole piece",* „Atomstrahl“*: "atomic ray".*
Figure taken from [10].

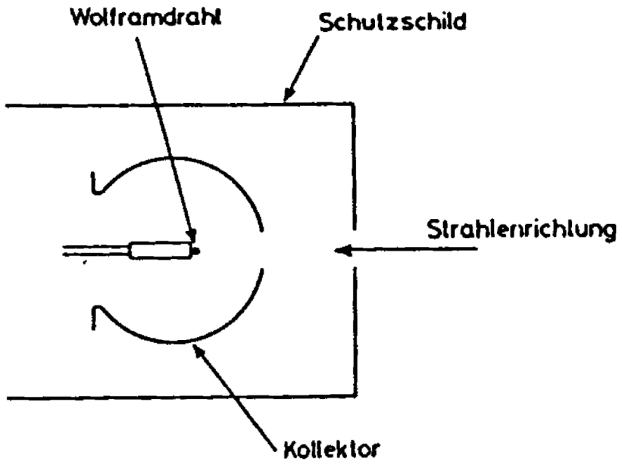

Figure 4: *Sketch of the Langmuir-Taylor detector. [15]*
The German words translate as follows: „Wolframdraht“*: "tungsten wire",* „Schutzschild“*: "protective shield",* „Strahlenrichtung“*: "direction of the ray",* „Kollektor“*: "collector".*

has to be introduced:

$$C' = (1-\epsilon)\,C = \left(1 - \frac{3r_1^2 - (r_1+h_1)^2}{(r_1^2 + (r_1+h_1)^2)^2}\; y^2\right) C. \tag{14}$$

The z-component of the magnetic field of the electromagnet can be calculated via

$$\begin{aligned} B_z(I) = (41.0 \pm 4.6)\,\mathrm{mT} + (436 \pm 30)\,\frac{\mathrm{mT}}{\mathrm{A}} \cdot I + \\ + (394 \pm 52)\,\frac{\mathrm{mT}}{\mathrm{A}^2} \cdot I^2 + (-203 \pm 24)\,\frac{\mathrm{mT}}{\mathrm{A}^3} \cdot I^3, \end{aligned} \tag{15}$$

which is the result of an old measurement [15]. There were no uncertainties provided and hence it was refrained from providing the (reduced) χ^2-value. The corresponding fit is shown in the appendix, see Figure A.2. This measurement has not been repeated for a long time and found to be off by about -5% [10]. Also note that, even though the magnet is demagnetized regularly there is a non-trivial value for $B_z(0)$. It is imperative to demagnetize the magnet regularly because of hysteresis effects, due to which a residual magnetization will remain when the current is turned off and Equation (15) cannot be used anymore. To achieve this, a strategy similar to that of pulse degaussing (cf. [16]) is used, which is visualized in Figure 5. After having used the magnet, the current is turned off, and after waiting for a brief period, a weaker current of opposite polarity is applied. Repeating this process successively diminishes the residual magnetization of the magnet. To test if the process was successful, a rod magnet can be held close to the magnet.

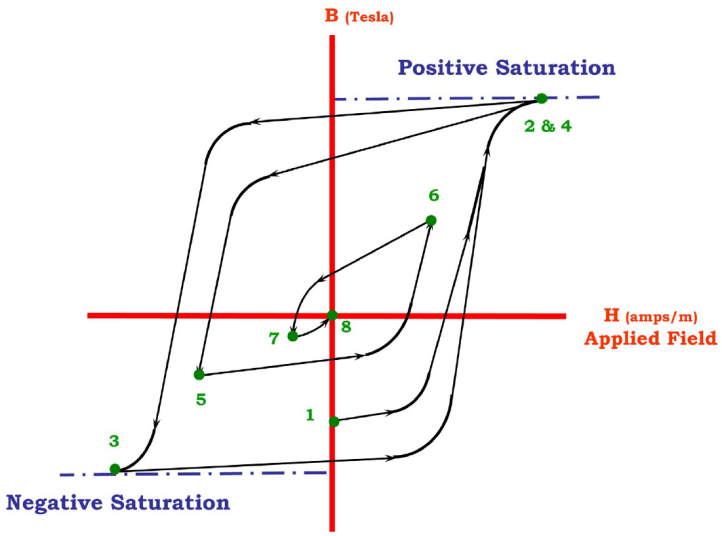

Figure 5: *The magnetization curve of a magnet which is subject to the process of pulse degaussing. [16]*

The LT-detector (Figure 4) can be shifted horizontally in this setup in order to measure the intensity distribution of the deflected potassium beam. It is supplied with a heating current and a collector voltage, both of which are adjustable. The heating current flows through the tungsten wire, which can raise its temperature above that at which potassium gets ionized. This is possible thanks to the comparatively

large ionization energy of tungsten, cf. [13, p. 1022] and [17]. Upon the ionization of the incoming potassium the collector will collect particles of one charge due to a potential difference caused by the collector voltage. This creates an electrical current proportional to the intensity of the incoming potassium atoms, which is measured with a Keithley Picoamperemeter. At this point it has to be mentioned that due to its working principle the detector suffers not only from a certain dead time and fluctuations, but also from residue that is deposited on the wire over time (e.g. potassium atoms). As a consequence the residue has to be cleaned off from time to time by heating the tungsten wire up, which is further described in Section 4.1.

For the resolution function of the LT-detector, we assume that it is a Voigt profile, given by

$$V(x;\mu,\sigma,\gamma) = (G * L)(x;\mu,\sigma,\gamma) = \int_{-\infty}^{\infty} G(x';\mu,\sigma)L(x-x';\mu,\gamma)\,\mathrm{d}x', \tag{16}$$

that is, a convolution of a Gaussian and a Lorentzian distribution

$$G(x;\mu,\sigma) = \frac{1}{\sigma\sqrt{2\pi}} e^{-\frac{(x-\mu)^2}{2\sigma^2}} \tag{17}$$

$$L(x;\mu,\gamma) = \frac{\gamma}{\pi((x-\mu)^2+\gamma^2)}, \tag{18}$$

with a shared center μ, Gaussian standard deviation σ and Lorentz scale parameter γ.

4 Measurements and Analysis

In this section, the measurements are described and the data taken will be discussed and analyzed.

Section 4.1 treats the preparations prior to the measurements, which will be discussed in the subsequent sections. In Section 4.2 the calibration of the Langmuir-Taylor detector as well as the measurement of its signal-to-noise ratio is explained. In Section 4.3 the conduction of the central experiment, the Stern-Gerlach experiment, is described: the intensity profile of the ray is measured after it has traveled through the magnetic field, whose field strength is varied, and from this profile the Landé factor g_e is determined. Finally, in Section 4.4, the measurement of the vaporization enthalpy of potassium is explained.

4.1 The Atomic Ray

Prior to taking measurements, the vacuum is examined using an ionization manometer. Measurements were carried out only at pressures between 6×10^{-9} bar and 5×10^{-8} bar to ensure accuracy, as the pressure was subject to fluctuations. Another preparatory task is to determine the temperature of the oven, which is measured using a PT100 resistor. Using the data given in [15] a quadratic fit is conducted, which yields

$$T(R) = (-243.8\pm0.1)\,^\circ\mathrm{C} + (2.328\pm0.001)\,\frac{^\circ\mathrm{C}}{\Omega}\cdot R + (1.109\pm0.003)\times10^{-3}\,\frac{^\circ\mathrm{C}}{\Omega^2}\cdot R^2 \tag{19}$$

where it was refrained from providing a reduced χ^2-value due to the lack of uncertainties. The corresponding fit is shown in the appendix, see Figure A.1. The motivation for the quadratic fit arises from the simplified Callendar–Van Dusen equation.

As mentioned before, on the surface of the tungsten wire residue of potassium or other gas molecules (which there were more of before the vacuum was created) may linger. For that reason the current of the tungsten wire is set to $\simeq 1.3\,\mathrm{A}$ for about 10 minutes so that the residue may be vaporized from the wire. (Note that this strategy, though stated like that in the manual [15], is ill-suited for this lab course and hence revised in the beginning of Section 4.3). This process has to be repeated after the detector has been exposed to the potassium ray for about 20 minutes, but otherwise the current of the tungsten wire remains at a value between 0.9 A and 1.0 A.

4.2 Configuration of the Langmuir-Taylor Detector

At a constant oven temperature of $(152.1 \pm 0.6)\,^\circ\mathrm{C}$, based on a measured resistance of $(158.1 \pm 0.2)\,\Omega$ and Equation (19), the signal of the LT-detector is measured for varying heating currents. The collector voltage is kept at $(20.0 \pm 0.1)\,\mathrm{V}$ and the measurement is carried out with and without the potassium ray, where in the former case the detector is moved into the roughly determined maximum. This allows to measure the signal to noise ratio and hence to determine an operating point. The heating current is varied in steps of 10 mA between 900 mA and 1040 mA. The results of the raw signal measurements with and without the beam can be seen in Figure 6 the resulting plot for the signal to noise ratio in Figure 7.

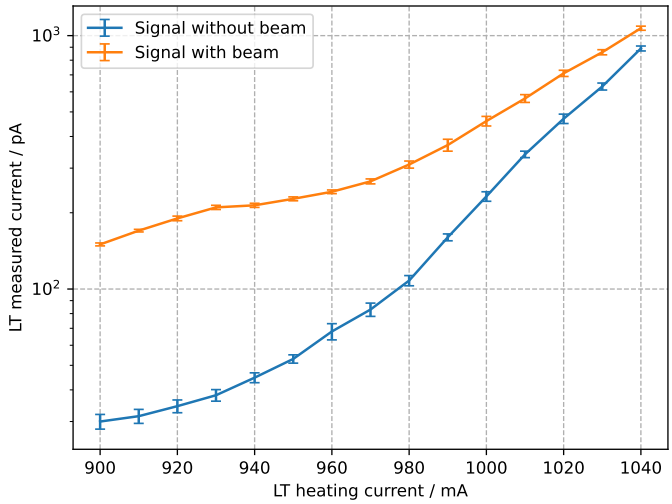

Figure 6: *Logarithmic plot of the raw measurements of signal intensity with and without the beam activated. A linear plot can be seen in Figure A.4. The underlying data is listed in Table B.1.*

While the operating point was first set to 950 mA based on the plot of the signal to noise ratio, upon recommendation of the supervisor it was set to 970 mA. This was done after having recorded data without the magnetic field as described in the following Section 4.3 with a heating current of 950 mA, the results of which can be seen in the

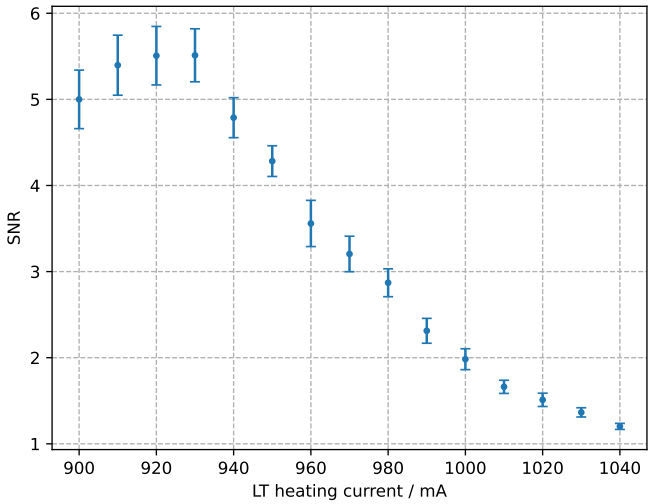

Figure 7: *Linear plot of the signal to noise ratio based on the data from the raw measurements as seen in Figure 6. A logarithmic plot can be seen in Figure A.3. The underlying data is listed in Table B.1.*

appendix in Figure A.5. The main reason behind this is that for larger heating currents the LT-detector suffers from a lower dead time.

4.3 Measurement of the Ray Profile and Splitting

With the working point set to 970 mA the profile of the beam is now measured. To that end the LT-detector is varied between 0.08 inches[4] and 0.33 inches, once without a magnetic field, and (upon consultation with the supervisor) for two different values of the magnetic field. The oven is again kept at a constant temperature throughout this series of measurements of $(152.1 \pm 0.6)\,°\mathrm{C}$. At this point it is worth mentioning that the strategy of measurement had to be adapted throughout the conduct of the experiment. The optimal signal could be recorded by heating the tungsten wire for no longer than a minute and subsequently turning off both heating current and collector voltage for 30 to 60 seconds. The latter part requires the presence of the supervisor as per the manual [15], as students are not allowed to turn on the heating current on their own. A longer burning period yielded a long period of significantly larger noise, which might mean that a longer burning period produces too much pollution, yielding a longer waiting time before the next measurement can be taken. This effect can be seen in the measurement which was taken shortly after a long burn of ca. seven minutes, see Figure A.6. As one can see the entire measurement is dominated by the linear decline after the burning.

Another such adaptation of the strategy was to manually ground the power supply unit of the oven. Not only did the experimenters receive electrical shocks on a regular basis, it was even the case that the noise was reduced upon grounding the device.

[4] $1\,\mathrm{inch} = 1\,\mathrm{in} = 1'' = 25.4\,\mathrm{mm}$

The values thus recorded can be seen in Figure 8. For the case of no magnetic field a Voigt profile (cf. Equation (16)), where the fit parameter γ is set equal to σ, with a constant underground is chosen as a fit function. It should be noted that other fit functions could have also been used as this fit itself does not contain any important physical parameters, as it rather serves to incorporate the limited resolution introduced by the detector.

Since the uncertainties of the measurements made were only roughly estimated, which was due to the strongly fluctuating and relatively slow updating display of the digital multimeter used to measure the current, the reduced χ^2-value of this fit has no meaningful significance. We therefore use the fit to determine the uncertainties of our measured values and select them in such a way that a reduced χ^2-value of 1 results, which generally speaks for well-chosen errors and fit models. To do this, the fit was repeated for a variety of different constant and relative errors such that the uncertainty σ_i of the i-th measurement value y_i is

$$\sigma_i = k + r \cdot y_i. \tag{20}$$

This resulted in the colour map of Figure 9, which shows the reduced χ^2 for each combination of absolute and relative error. Since we have two parameters with which we can influence the reduced χ^2, there is a range of possible combinations for which the reduced χ^2 is equal to 1, see the red line in Figure 9. For simplicity, we choose $k = 5\,\mathrm{pA}$ as the constant error and the corresponding $r = 6.5\,\%$ as the relative error, since it seems to be roughly in the middle of the extreme cases, i.e. no relative error or no absolute error, which lead to under- resp. overweighting of the tails.
For this choice of uncertainties, $k = 5\,\mathrm{pA}$ and $r = 6.5\,\%$, the reduced χ^2-value is 0.988 and the resulting fit can be seen in Figure 8.

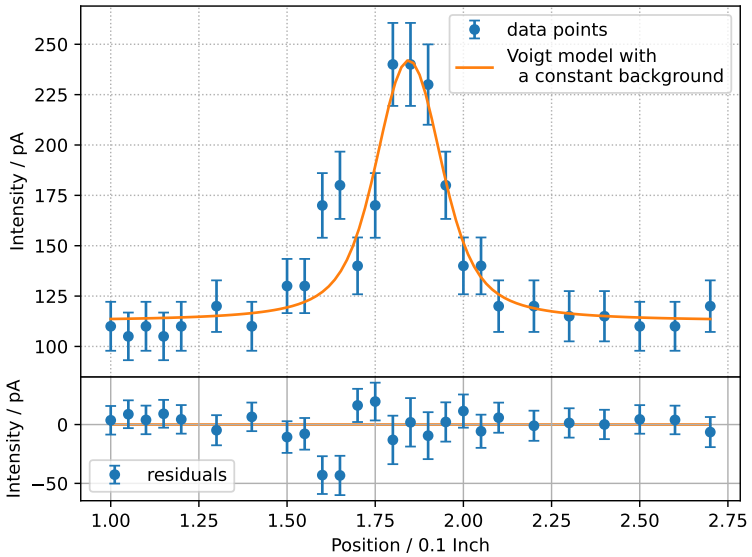

Figure 8: *Fit of a Voigt model with a constant background to the beam intensity recorded with no magnetic field applied in order to determine the resolution function. The fit parameters are the following amplitude:* 38.42 ± 4.30 *center:* 1.84 ± 0.01 *sigma:* 0.06 ± 0.01 *c:* 112.5 ± 3.4

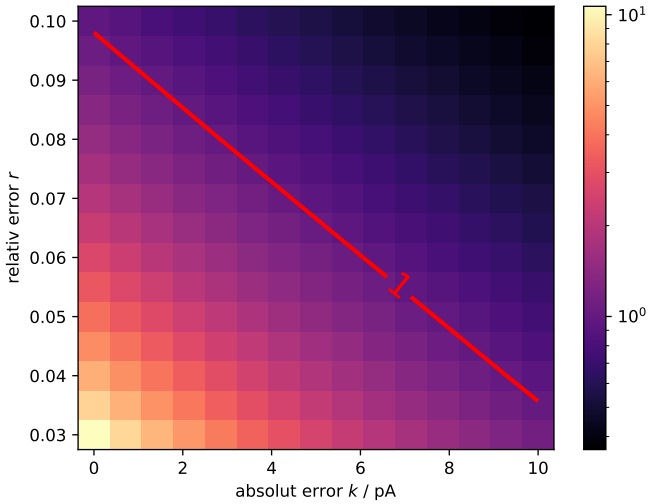

Figure 9: *A colour map depicting the different reduced χ^2 for diffrent combinations of relativ and abolut erros in the fit of the resolution function. The red line indicates all the combiations leading to a reduced χ^2 of 1.*

The resulting Voigt profile $V(z)$ – the fit function without the constant underground – is then integrated[5] to yield the normalized resolution function

$$R(\tilde{z}) = \begin{cases} \left(\int_{-\infty}^{\infty} V(z')\,\mathrm{d}z'\right)^{-1} V(\tilde{z}+\mu) & 0.1'' \leq \tilde{z}+\mu \leq 0.27'' \\ 0 & \text{otherwise} \end{cases} \tag{21}$$

where μ is the center of the Voigt profile. This shift is done to ensure that the maximum of R is at 0 because the detector resolution in the following convolution depends only on the distance of the convoluted points. R is then used as the resolution function for measurements with a non-trivial magnetic field to account for any smearing of the expected distribution due to the detector. The fit function for the measured data with a non-trivial magnetic field is therefore (cf. Equations (9), (12), (16) and (21))

$$F(x) = (R * h)(z; g_e, O) \cdot A + mz + b = h_{\text{meas}}(z - O; g_e) \cdot A + mz + b. \tag{22}$$

$(R * h)$ stands for the convolution of the resolution function R and the theoretically expected distribution h, which solely depends on Landé factor g_e (apart from external quantities like the magnetic field and the temperature of the oven). The additional linear term with slope m and offset b accounts for the background noise. O denotes the offset with regards to the center of the beam and A is a general amplitude with which the convoluted function is multiplied. The parameters defining the resolution function V can be seen in the caption of Figure 8. By means of this fit function we can therefore determine the Landé factor g_e.

However, when neglecting the resolution of the detector and using the peak positions at face value, one is already able to approximately compute g_e. For this, the peak

[5]The integration does not have to done explicitly because the amplitude yielded from the fit in Figure 8 is the area under the Voigt profile from $-\infty$ to ∞.

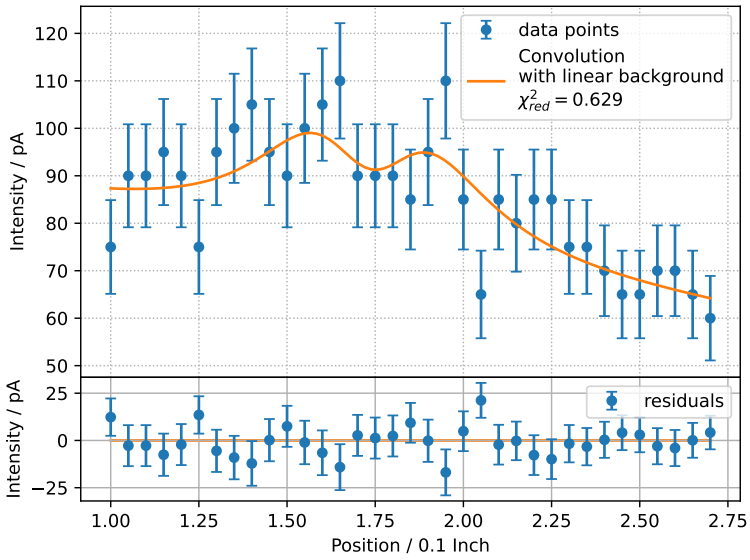

Figure 10: *Intensity measurement of the beam with a magnetic field of* $(0.329 \pm 0.021)\,\mathrm{T}$*, based on a observed current of* $0.496\,\mathrm{A}$*. All fit parameters are displayed in Table 2 while the underlying data is listed in Table B.2.*

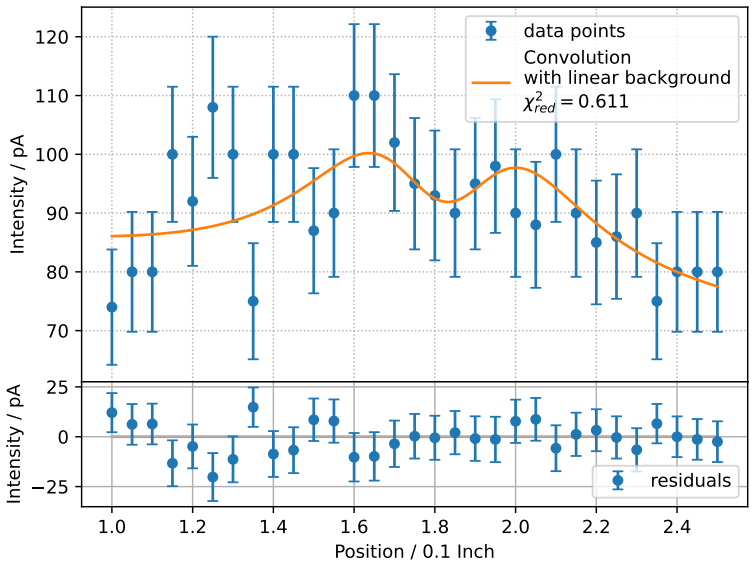

Figure 11: *Repeated intensity measurement of the beam with a magnetic field of* $(0.329 \pm 0.021)\,\mathrm{T}$*, based on a observed current of* $0.496\,\mathrm{A}$*. All fit parameters are displayed in Table 2 while the underlying data is listed in Table B.2.*

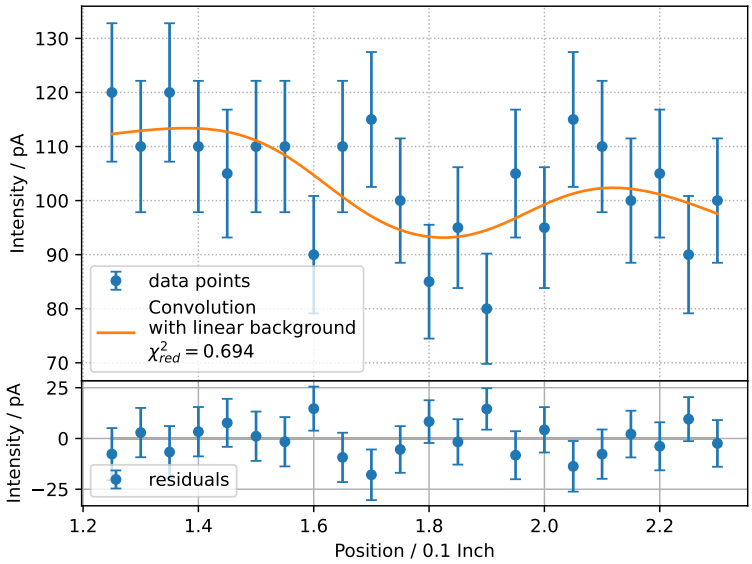

Figure 12: *Intensity measurement of the beam with a magnetic field of* $(0.501 \pm 0.038)\,\mathrm{T}$*, based on a observed current of* $0.746\,\mathrm{A}$*.All fit parameters are displayed in Table 2 while the underlying data is listed in Table B.2.*

Table 1: *Values of* g_e *determined from peak positions of the measured intensity profiles at different magnetic fields. The uncertainties were chosen to be equal to the step sizes in which the position of the LT detector was changed.*

I/mA	$z_{\max}^{\mathrm{left}}/0.1\,\mathrm{in}$	$z_{\max}^{\mathrm{right}}/0.1\,\mathrm{in}$	g_e^{naive}
496	1.65 ± 0.05	1.95 ± 0.05	1.10 ± 0.27
496	1.625 ± 0.05	1.95 ± 0.05	1.19 ± 0.27
746	1.70 ± 0.05	2.05 ± 0.05	0.84 ± 0.18
		Combined g_e^{naive}	1.05 ± 0.14

positions where determined by hand. The selected locations and the resulting Landé factors are shown in Table 1. The figures with the data from which the peak positions where manually determined are Figures 10 to 12. It should be noted that the measurement at a magnetic field of $(0.329 \pm 0.021)\,\mathrm{T}$ was made twice to confirm that the data actually contained large fluctuations and was not a one-off event. After this only one additional measurement was taken at a magnetic field of $(0.501 \pm 0.038)\,\mathrm{T}$. This is partly due to the time constraints, but also because further increasing the magnetic field would make the peaks indistinguishable from the background, and decreasing the magnetic field would make the peaks indistinguishable from each other.

The fit function in these figures has the form of Equation (22). All fit parameters, including the Landé factor, are shown in Table 2. Within the errors of the fit parameters the amplitude, i.e the the total intensity of the beam, and the location of the beam center are constant. The final combined measurements of the Landé factor form the three fits is

$$g_e^{\mathrm{total}} = 1.16 \pm 0.16.$$

Table 2: *Values of g_e determined from the fits of the measured intensity profiles at different magnetic fields. The underlying data is listed in Table B.2.*

I/mA	B/mT	b/pA	$m/10\,\mathrm{pA/in}$	A	$O/0.1\,\mathrm{in}$	g_e
496	329 ± 21	74.1 ± 3.2	-12.8 ± 3.3	28.9 ± 6.1	1.74 ± 0.05	0.91 ± 0.19
496	329 ± 21	77.8 ± 4.2	-6.8 ± 4.1	26.5 ± 6.9	1.83 ± 0.05	1.04 ± 0.21
746	501 ± 38	88.1 ± 7.6	-15.2 ± 6.7	18.6 ± 9.6	1.79 ± 0.05	1.54 ± 0.42
					Combined g_e	1.16 ± 0.16

This estimate of the Landé factor deviates approximately 72% from the theoretically expected and in experiments measured value. In terms of standard deviation the difference is 5.26σ. A obvious reason for the discrepancy is the poor quality of the measured data which in turn is a result of various fault of the experiment setup such as but not limited to the vacuum pump, the leaky setup or the requirement of manually evaluating the intensity via a strongly fluctuating multimeter. This statement is also supported by the low signal-to-noise ratio (cf. Section 4.2). Additionally, the error is probably underestimated as the least squares method of fitting to the measured intensity does not account for uncertainties in the underlying fitting function. Since the fitting function in this experiment is influenced by, for example, the temperature of the oven or the strength of the magnetic field, which have both a statistical and a significant unknown systematic error, the actual error in the measured Landé factor is certainly greater. One possible method of taking this into account is by repeating the fit, where each time the value for the magnetic field and temperature is drawn from a Gaussian distribution with the center at the expected value and the standard deviation at the respective error. However, as the fitting process already takes a long time due to the computationally expensive procedure, this method is too time expensive for the time frame of this experiment.

4.4 Measurement of the Vapor Pressure of Potassium

As final measurement, the vapor pressure of potassium is measured. To that end, after demagnetizing the magnet, the oven is heated to about 190 °C and thereafter turned off. The aperture is opened and the beam intensity in the maximum is measured with the LT-detector in dependence of the temperature, which decreases over time. The integrated form of the Clausius-Clapeyron equation (see e.g. [18]) yields a fit function of the form

$$U(\beta) = U_0 e^{-\beta H} + U_b, \tag{23}$$

where $\beta = (k_B T)^{-1}$ with T in Kelvin, H is the enthalpy of evaporation and U_b is a constant that accounts for the background. Note that due to friction one expects a deviation from the Clausius-Clapeyron equation at high temperatures (low β)[15], and due to a bad signal to noise ratio for low temperatures (high β) as well, which is why only a certain range is fitted in Figure 13. The literature value for the enthalpy of evaporation of potassium is about 76.9 kJ/mol [19], which translates to about 0.797 eV per atom.

While the parameters form U_b and U_0 from the fit have large relative errors, the fit was able to determine the enthalpy with a relative error of less than 10%. The

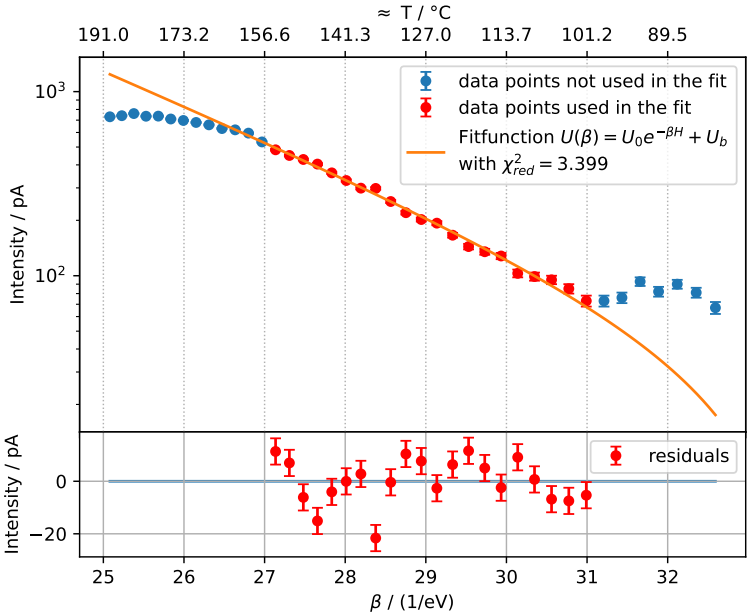

Figure 13: *Fit of the measured data with the fit function from Equation (23). Only a manually selected region, as seen, is fitted. The resulting fit parameters are:* $U_b = (-33.1 \pm 19.6)\,\mathrm{pA}$, $U_0 = (6.0 \pm 5.2) \times 10^7\,\mathrm{pA}$ *and* $H = (0.43 \pm 0.03)\,\mathrm{eV}$. *The underlying data can be seen in Table B.3*

enthalpy based on the measured data is $(0.42 \pm 0.03)\,\mathrm{eV}$. While the measured value of the enthalpy is significaly off from the theoreticly expecteed enthalpy of evaporation of potassium, the ability to fit a exponential function of the from Equation (23), demonstrates that the oven was roughly between 156 °C and 101 °C in thermal equilibrium. This shows that the operating temperature in the Landé factor measurement, where it was kept at a constant temperature of $(152.1 \pm 0.6)\,°\mathrm{C}$, was in the range where the oven is in thermal equilibrium.

5 Summary

The aim of this experiment was the demonstration of the quantization of the spin of the electron as well as the measurement of the Landé factor g_e. To that end a modified Ealing-Daybell Stern-Gerlach apparatus was used and operated with potassium and a Langmuir-Taylor (LT)-detector. In addition, the experiment is designed to determine the vaporization enthalpy of potassium.

It was expected that the potassium ray would be split in two equal parts by the Stern-Gerlach apparatus. The data recorded only allows to speculate in that regard, as it was dominated by noise and only weakly showed the characteristic of two global maxima of the intensity spectrum even with a comparatively strong magnetic field. The fits converged nonetheless and yielded a total value of

$$g_e^{\text{total}} = 1.16 \pm 0.16,$$

which deviates by 72 %, resp. 5.26σ, from the literature value of $g_e = 2.002\,319\,304\,362\,2(15)$ [4]. This may be due to strong fluctuations of the LT-detector signal during measurements and the improper vacuum. In addition, the instructions of the manual [15] were partially found to be inappropriate for some measurements, and there is reason to believe that part of the experiment is not grounded properly. It should also be mentioned that the error of the measured Landé factor is an underestimate of the true error, since, for example, the error of the magnetic field and the oven temperature could not be included in the errors extracted from the fit.

By means of the Clausius-Clapeyron equation it was attempted to measure the vaporization enthalpy of potassium. The result is

$$H = (0.43 \pm 0.03)\,\text{eV},$$

which significant deviates from the literature value of approximately 0.797 eV. However, the temperature at which the oven was set to measure the Landé factor, $(152.1 \pm 0.6)\,^\circ\text{C}$, is in the range where the intensity follows the exponential decay, showing that the oven was in thermal equilibrium throughout the experiment.

Overall the evidence seems to indicate that the equipment is currently not well-suited to conduct this experiment and may need a comprehensive examination and recalibration to find the leaks in the vacuum and to reduce the unknown systematic errors of the temperature and magnetic field strength. In addition, a thorougher understanding of the systematic errors is needed, based on the observation that the Landé factor has been greatly underestimated compared to the precisely determined literature value.

A Further Data

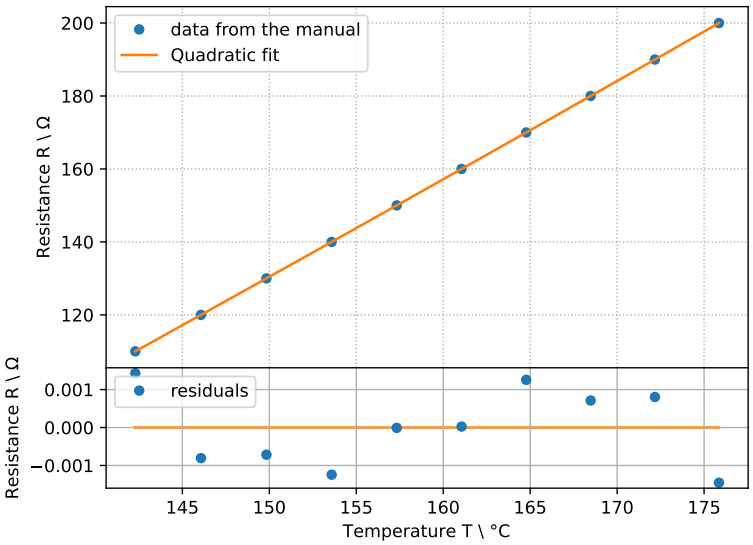

Figure A.1: *Fitting of the temperature resistance curve based on the data in the supplied manual.*

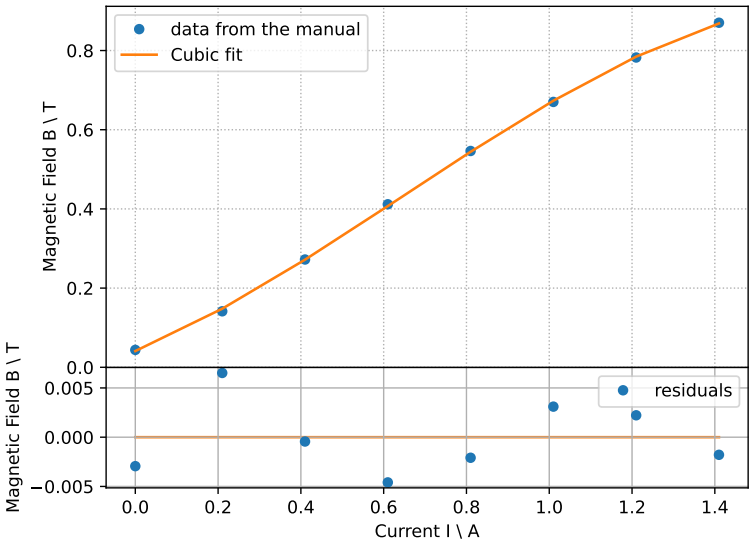

Figure A.2: *Fitting of the magnetic field and current curve based on the data in the supplied manual.*

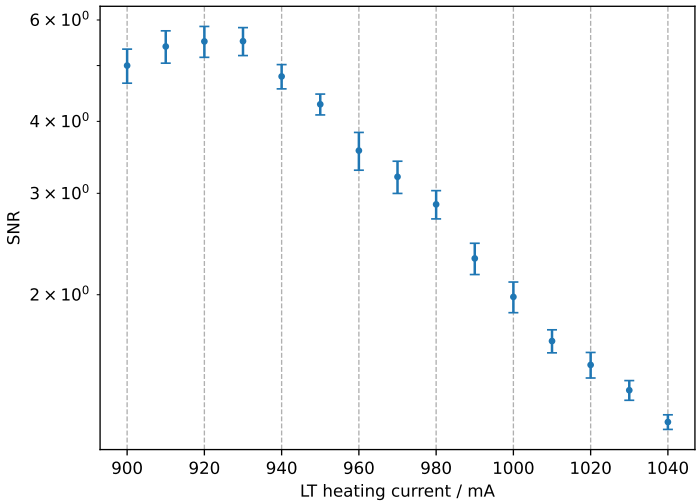

Figure A.3: *Logarithmic plot of the signal to noise ratio based on the data from the raw measurements as seen in Figure 6.*

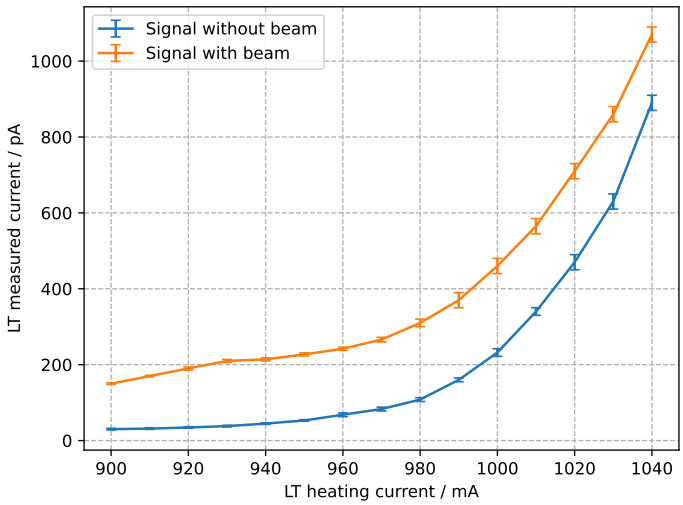

Figure A.4: *Linear plot of the raw measurements of signal intensity with and without the beam activated.*

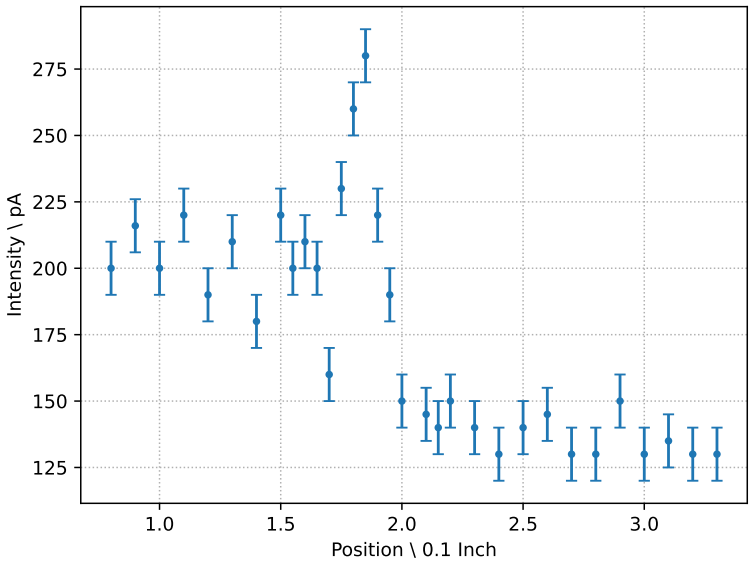

Figure A.5: *Raw data recorded while the heating current was set to* $950\,\mathrm{mA}$.

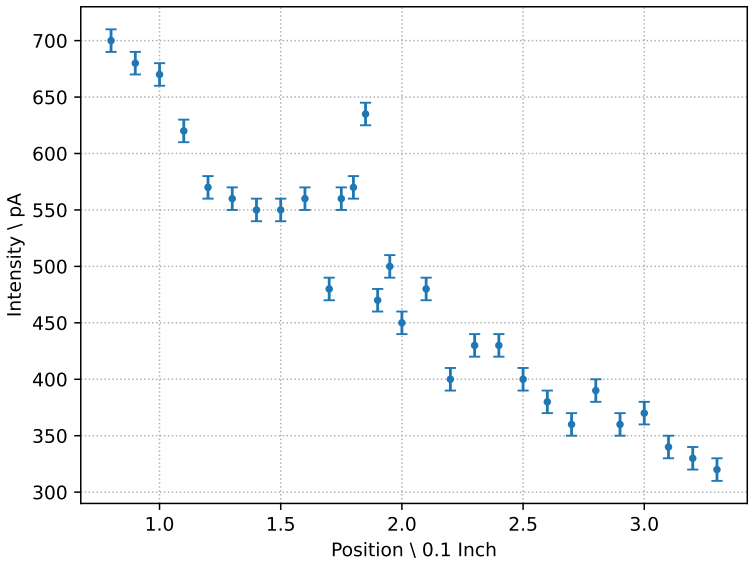

Figure A.6: *Measurement taken directly taken after a long burn.*

B Full Measurements

Table B.1: *Data form the measurement the signal with and without the beam present and no magnetic field to determine the signal to noise ratio*

I_{heat}/mA	Intensity without beam/pA		Intensity with beam/pA		SNR	
900	30.0 $\pm$	2.0	150.0 $\pm$	2.0	5.0	$\pm$ 0.34
910	31.5 $\pm$	2.0	170.0 $\pm$	2.0	5.4	$\pm$ 0.35
920	34.5 $\pm$	2.0	190.0 $\pm$	4.0	5.5	$\pm$ 0.34
930	38.1 $\pm$	2.0	210.0 $\pm$	4.0	5.5	$\pm$ 0.31
940	44.7 $\pm$	2.0	214.0 $\pm$	4.0	4.8	$\pm$ 0.23
950	53.0 $\pm$	2.0	227.0 $\pm$	4.0	4.3	$\pm$ 0.18
960	68.0 $\pm$	5.0	242.0 $\pm$	4.0	3.6	$\pm$ 0.27
970	83.0 $\pm$	5.0	266.0 $\pm$	6.0	3.2	$\pm$ 0.21
980	108.0 $\pm$	5.0	310.0 $\pm$	10.0	2.9	$\pm$ 0.16
990	160.0 $\pm$	5.0	370.0 $\pm$	20.0	2.3	$\pm$ 0.14
1000	232.0 $\pm$	10.0	460.0 $\pm$	20.0	2.0	$\pm$ 0.12
1010	340.0 $\pm$	10.0	565.0 $\pm$	20.0	1.7	$\pm$ 0.08
1020	470.0 $\pm$	20.0	710.0 $\pm$	20.0	1.5	$\pm$ 0.08
1030	630.0 $\pm$	20.0	860.0 $\pm$	20.0	1.4	$\pm$ 0.05
1040	890.0 $\pm$	20.0	1070.0 $\pm$	20.0	1.2	$\pm$ 0.04

Table B.2: *Data form the measurement of the ray profile and splitting. The detector position z is assumed to be errorless for simplicity. Not in all measurement series data was taken for all z-values due to time constraints such that points in the tails of the intensity distributions were left out.*

$z/0.1\,\mathrm{in}$	Intensity/pA			
	$I = 0\,\mathrm{mA}$ $B = 0\,\mathrm{mT}$	$I = 496\,\mathrm{mA}$ $B = 329\,\mathrm{mT}$	$I = 496\,\mathrm{mA}$ $B = 329\,\mathrm{mT}$	$I = 746\,\mathrm{mA}$ $B = 501\,\mathrm{mT}$
1.00	110.0 ± 12.2	75.0 ± 9.9	74.0 ± 9.8	
1.05	105.0 ± 11.8	90.0 ± 10.9	80.0 ± 10.2	
1.10	110.0 ± 12.2	90.0 ± 10.9	80.0 ± 10.2	
1.15	105.0 ± 11.8	95.0 ± 11.2	100.0 ± 11.5	
1.20	110.0 ± 12.2	90.0 ± 10.9	92.0 ± 11.0	
1.25		75.0 ± 9.9	108.0 ± 12.0	120.0 ± 12.8
1.30	120.0 ± 12.8	95.0 ± 11.2	100.0 ± 11.5	110.0 ± 12.2
1.35		100.0 ± 11.5	75.0 ± 9.9	120.0 ± 12.8
1.40	110.0 ± 12.2	105.0 ± 11.8	100.0 ± 11.5	110.0 ± 12.2
1.45		95.0 ± 11.2	100.0 ± 11.5	105.0 ± 11.8
1.50	130.0 ± 13.5	90.0 ± 10.9	87.0 ± 10.7	110.0 ± 12.2
1.55	130.0 ± 13.5	100.0 ± 11.5	90.0 ± 10.9	110.0 ± 12.2
1.60	170.0 ± 16.1	105.0 ± 11.8	110.0 ± 12.2	90.0 ± 10.9
1.65	180.0 ± 16.7	110.0 ± 12.2	110.0 ± 12.2	110.0 ± 12.2
1.70	140.0 ± 14.1	90.0 ± 10.9	102.0 ± 11.6	115.0 ± 12.5
1.75	170.0 ± 16.1	90.0 ± 10.9	95.0 ± 11.2	100.0 ± 11.5
1.80	240.0 ± 20.6	90.0 ± 10.9	93.0 ± 11.0	85.0 ± 10.5
1.85	240.0 ± 20.6	85.0 ± 10.5	90.0 ± 10.9	95.0 ± 11.2
1.90	230.0 ± 20.0	95.0 ± 11.2	95.0 ± 11.2	80.0 ± 10.2
1.95	180.0 ± 16.7	110.0 ± 12.2	98.0 ± 11.4	105.0 ± 11.8
2.00	140.0 ± 14.1	85.0 ± 10.5	90.0 ± 10.9	95.0 ± 11.2
2.05	140.0 ± 14.1	65.0 ± 9.2	88.0 ± 10.7	115.0 ± 12.5
2.10	120.0 ± 12.8	85.0 ± 10.5	100.0 ± 11.5	110.0 ± 12.2
2.15		80.0 ± 10.2	90.0 ± 10.9	100.0 ± 11.5
2.20	120.0 ± 12.8	85.0 ± 10.5	85.0 ± 10.5	105.0 ± 11.8
2.25		85.0 ± 10.5	86.0 ± 10.6	90.0 ± 10.9
2.30	115.0 ± 12.5	75.0 ± 9.9	90.0 ± 10.9	100.0 ± 11.5
2.35		75.0 ± 9.9	75.0 ± 9.9	
2.40	115.0 ± 12.5	70.0 ± 9.6	80.0 ± 10.2	
2.45		65.0 ± 9.2	80.0 ± 10.2	
2.50	110.0 ± 12.2	65.0 ± 9.2	80.0 ± 10.2	
2.55		70.0 ± 9.6		
2.60	110.0 ± 12.2	70.0 ± 9.6		
2.65		65.0 ± 9.2		
2.70	120.0 ± 12.8	60.0 ± 8.9		

Table B.3: *Cooling down data. The measured values are the resistance of the oven to determine its temperature and the corresponding beam intensity measured as current. The calculated temperature T and the inverse temperature $\beta = 1/k_B T$ are also given.*

R_{oven}/Ω	Intensity/pA	$T/^{\circ}\text{C}$	β/eV^{-1}
172	730 ± 5	189.53 ± 0.25	25.081 ± 0.013
171	740 ± 5	186.82 ± 0.24	25.229 ± 0.013
170	760 ± 5	184.12 ± 0.24	25.378 ± 0.013
169	735 ± 5	181.41 ± 0.24	25.529 ± 0.014
168	736 ± 5	178.71 ± 0.24	25.682 ± 0.014
167	710 ± 5	176.01 ± 0.24	25.836 ± 0.014
166	697 ± 5	173.31 ± 0.24	25.992 ± 0.014
165	680 ± 5	170.62 ± 0.24	26.150 ± 0.014
164	660 ± 5	167.92 ± 0.23	26.310 ± 0.014
163	630 ± 5	165.23 ± 0.23	26.471 ± 0.014
162	620 ± 5	162.54 ± 0.23	26.635 ± 0.014
161	595 ± 5	159.85 ± 0.23	26.800 ± 0.014
160	533 ± 5	157.17 ± 0.23	26.967 ± 0.014
159	483 ± 5	154.49 ± 0.23	27.136 ± 0.014
158	450 ± 5	151.81 ± 0.23	27.307 ± 0.014
157	428 ± 5	149.13 ± 0.22	27.481 ± 0.015
156	404 ± 5	146.45 ± 0.22	27.656 ± 0.015
155	362 ± 5	143.78 ± 0.22	27.833 ± 0.015
154	329 ± 5	141.11 ± 0.22	28.013 ± 0.015
153	299 ± 5	138.44 ± 0.22	28.194 ± 0.015
152	298 ± 5	135.77 ± 0.22	28.378 ± 0.015
151	253 ± 5	133.11 ± 0.22	28.564 ± 0.015
150	220 ± 5	130.45 ± 0.21	28.753 ± 0.015
149	202 ± 5	127.79 ± 0.21	28.944 ± 0.015
148	193 ± 5	125.13 ± 0.21	29.137 ± 0.015
147	166 ± 5	122.47 ± 0.21	29.332 ± 0.016
146	144 ± 5	119.82 ± 0.21	29.530 ± 0.016
145	135 ± 5	117.17 ± 0.21	29.731 ± 0.016
144	128 ± 5	114.52 ± 0.21	29.934 ± 0.016
143	103 ± 5	111.87 ± 0.20	30.140 ± 0.016
142	99 ± 5	109.23 ± 0.20	30.348 ± 0.016
141	95 ± 5	106.58 ± 0.20	30.560 ± 0.016
140	85 ± 5	103.94 ± 0.20	30.774 ± 0.016
139	73 ± 5	101.31 ± 0.20	30.990 ± 0.017
138	73 ± 5	98.67 ± 0.20	31.210 ± 0.017
137	76 ± 5	96.04 ± 0.20	31.433 ± 0.017
136	93 ± 5	93.41 ± 0.20	31.658 ± 0.017
135	82 ± 5	90.78 ± 0.19	31.887 ± 0.017
134	90 ± 5	88.15 ± 0.19	32.119 ± 0.017
133	81 ± 5	85.52 ± 0.19	32.354 ± 0.017
132	67 ± 5	82.90 ± 0.19	32.592 ± 0.017

C Gaussian Error Propagation

More often than not the experiment does not measure the desired quantity directly, but rather some primary variables (a voltage, time, an electric current, ...), from which the quantity in question can be computed. In that case, naturally the error of that quantity has to be determined, too. If the measurements of the primary observables are identically independently Gaussian distributed, one may approximate the uncertainty of the composite quantity via

$$\Delta f(x, y, ...) = \sqrt{\left((\Delta x)^2 \frac{\partial f}{\partial x}\right)^2 + \left((\Delta y)^2 \frac{\partial f}{\partial y}\right)^2 + ...},$$

where $x, y, ...$ are the aforementioned primary observables, $f(x, y, ...)$ the aforementioned composite quantity and Δ indicates the uncertainty of the respective quantity. This is called Gaussian error propagation.

References

[1] Walther Gerlach and Otto Stern. "Der experimentelle Nachweis der Richtungsquantelung im Magnetfeld". In: *Zeitschrift für Physik* 9.1 (Dec. 1, 1922), pp. 349–352. ISSN: 0044-3328. DOI: 10.1007/BF01326983. URL: https://doi.org/10.1007/BF01326983.

[2] Walther Gerlach and Otto Stern. "Über die Richtungsquantelung im Magnetfeld". In: *Annalen der Physik* 379.16 (1924), pp. 673–699. DOI: https://doi.org/10.1002/andp.19243791602. eprint: https://onlinelibrary.wiley.com/doi/pdf/10.1002/andp.19243791602. URL: https://onlinelibrary.wiley.com/doi/abs/10.1002/andp.19243791602.

[3] *100 Jahre Stern-Gerlach-Experiment*. Press release. Deutsche Physikalische Gesellschaft e. V., Feb. 4, 2022. URL: https://www.dpg-physik.de/veroeffentlichungen/aktuell/2022/100-jahre-stern-gerlach-experiment (visited on 01/27/2024).

[4] Wolfgang Demtröder. *Experimentalphysik 3 Atome, Moleküle und Festkörper*. Springer-Verlag, 2016.

[5] Mark Thomson. *Modern Particle Physics*. Cambridge University Press, 2013. ISBN: 978-1-107-03426-6.

[6] T. Albahri et al. "Measurement of the anomalous precession frequency of the muon in the Fermilab Muon $g-2$ Experiment". In: *Phys. Rev. D* 103 (7 Apr. 2021), p. 072002. DOI: 10.1103/PhysRevD.103.072002. URL: https://link.aps.org/doi/10.1103/PhysRevD.103.072002.

[7] B. Abi et al. "Measurement of the Positive Muon Anomalous Magnetic Moment to 0.46 ppm". In: *Phys. Rev. Lett.* 126 (14 Apr. 2021), p. 141801. DOI: 10.1103/PhysRevLett.126.141801. URL: https://link.aps.org/doi/10.1103/PhysRevLett.126.141801.

[8] D. P. Aguillard et al. "Measurement of the Positive Muon Anomalous Magnetic Moment to 0.20 ppm". In: *Phys. Rev. Lett.* 131 (16 Oct. 2023), p. 161802. DOI: 10.1103/PhysRevLett.131.161802. URL: https://link.aps.org/doi/10.1103/PhysRevLett.131.161802.

[9] Sz. Borsanyi et al. "Leading hadronic contribution to the muon magnetic moment from lattice QCD". In: *Nature* 593.7857 (May 1, 2021), pp. 51–55. ISSN: 1476-4687. DOI: 10.1038/s41586-021-03418-1. URL: https://doi.org/10.1038/s41586-021-03418-1.

[10] K. Hamacher. *Musterprotokoll FP 1 Stern-Gerlach Experiment*. https://moodle.uni-wuppertal.de/pluginfile.php/1102208/mod_resource/content/3/document.pdf.

[11] A. Klümper. *Fortgeschrittene Quantenmechanik. Vorlesung an der Bergischen Universität Wuppertal, Wintersemester 2021/22*.

[12] L. Spieß et al. *Moderne Röntgenbeugung*. Vieweg + Teubner GWV Fachverlage GmbH, 2009.

[13] G. W. F. Drake. *Springer Handbook of Atomic, Molecular, and Optical Physics*. Springer Nature Switzerland AG, 2023.

[14] *Description of the Ealing-Daybell Stern-Gerlach Apparatus*. https://moodle.uni-wuppertal.de/mod/folder/view.php?id=319159.

[15] *Anleitung zum Stern–Gerlach–Versuch*. https://moodle.uni-wuppertal.de/pluginfile.php/1102206/mod_resource/content/3/STG-Anleitung.pdf.

[16] John J. Holmes. *Reduction of a Ship's Magnetic Field Signatures*. Springer Nature Switzerland AG, 2022.

[17] H. A. Klein H. P. Latscha. *Anorganische Chemie*. Springer-Verlag Berlin Heidelberg, 2002, p. 44.

[18] W. Nolting. *Grundkurs Theoretische Physik 6 Statistische Physik*. Springer-Verlag Berlin Heidelberg, 2014.

[19] *19K Kalium engl. Potassium*. Accessed over The Web Archive. Nov. 13, 2004. URL: https://web.archive.org/web/20041113102953/http://www.lev.shuttle.de/lev/whs/ELEMENTE/el19.htm%5C#konf (visited on 01/27/2024).